



## Synergistic effect of artificial enzyme and 2D nano-structured $\text{Bi}_2\text{WO}_6$ for eco-friendly and efficient biomimetic photocatalysis



Huan Yi<sup>a,b,1</sup>, Ming Yan<sup>a,b,1</sup>, Danlian Huang<sup>a,b,1</sup>, Guangming Zeng<sup>a,b,\*</sup>, Cui Lai<sup>a,b,\*</sup>, Minfang Li<sup>a,b</sup>, Xiuqin Huo<sup>a,b</sup>, Lei Qin<sup>a,b</sup>, Shiyu Liu<sup>a,b</sup>, Xigui Liu<sup>a,b</sup>, Bisheng Li<sup>a,b</sup>, Han Wang<sup>a,b</sup>, Maocai Shen<sup>a,b</sup>, Yukui Fu<sup>a,b</sup>, Xueying Guo<sup>a,b</sup>

<sup>a</sup> College of Environmental Science and Engineering, Hunan University, Changsha, Hunan 410082, China

<sup>b</sup> Key Laboratory of Environmental Biology and Pollution Control (Hunan University), Ministry of Education, Changsha, Hunan 410082, China

### ARTICLE INFO

**Keywords:**  
Artificial enzyme  
Hemin  
Two dimension  
 $\text{Bi}_2\text{WO}_6$   
Photocatalysis

### ABSTRACT

Highly-efficient and eco-friendly materials and technologies are urgently needed to meet the requirements of nowadays green development. Photocatalysis with using solar energy and enzymatic catalysis with eco-friendly nature are effective alternatives to address the problem. Notably, beneficial use of the synergistic effect of artificial enzyme and advanced photocatalyst has attracted wide attention. This work presents a biomimetic photocatalytic material, two-dimensional (2D) biomimetic hemin-bismuth tungstate (HBWO). Stable HBWO composites formed by immobilization of monomeric hemin on 2D bismuth tungstate layer, exhibit high photocatalytic performance, better than that of pure 2D bismuth tungstate and unsupported hemin. HBWO shows layered structure with the interlayer spacing at  $\sim 0.35$  nm. In the photocatalytic process, hemin can not only act as an electron shuttle, also play an important role in oxygen transfer. Additionally, the synthesized HBWO composites exhibit nice binding affinities and high photocatalytic activity in tetracycline degradation. It is anticipated that beneficial use of synergistic effect of artificial enzyme and photocatalyst via HBWO composites can be a promising eco-friendly and efficient solution for addressing the environmental crisis.

### 1. Introduction

Enzymes are well-known to show high catalytic activity, and have been used in addressing energy and environmental crisis for decades [1–10]. However, the practical application of enzymes is limited by the low operational stability, harsh environmental conditions and expensive preparation process [11–16]. To satisfy the needs of the scientific development, the design and promotion of artificial enzymes is developed rapidly [17–21]. Hemin, an attractive biomimetic material, is a promising material for preparation of artificial enzymes, like graphene-hemin, G-quadruplex/hemin and hemin-AO-PAN [22–24]. Up to date, hemin has been well studied as catalysts because of their unique physicochemical behavior, especially high conductivity [25–28]. The catalytic performance of hemin is largely influenced by the electron transfer between the central iron and substances [29]. Hemin can play an important role in electron transfer in the catalytic process. Moreover, hemin has been proved to be an oxygen transfer reagent [30,31]. Nevertheless, monomeric hemin in solution is easy to aggregate to form

inactive dimers, which has a negative effect in the catalytic performance. Efficient methods to maintain the activity of monomeric hemin are urgently needed.

In recent years, many methods have been developed, especially the immobilization process [32–35]. For example, Huang et al. [36] used graphene as the support to immobilize hemin to be a highly biomimetic oxidation catalyst, showing high catalytic activity for the pyrogallol oxidation reaction with  $\text{H}_2\text{O}_2$ . Pyrogallol was oxidized to purpurogallin with catalytic efficiency at  $2.0 \times 10^5 \text{ M}^{-1} \text{ min}^{-1}$ . Yao et al. [29] introduced multi-walled carbon nanotubes to improve the catalytic performance of hemin on methylene blue degradation with the assistance of  $\text{H}_2\text{O}_2$ . The elimination kinetics reached  $0.04195 \text{ min}^{-1}$ . Lu et al. [37] combined  $\text{g-C}_3\text{N}_4$  with hemin via axial coordination to degrade 4-chlorophenol, which not only maintained the stability of hemin but also improved the photocatalytic performance of  $\text{g-C}_3\text{N}_4$ , but it is worth noting that 4-chlorophenol degradation efficiency was reduced 72% without  $\text{H}_2\text{O}_2$  compared with that in the presence of  $\text{H}_2\text{O}_2$ .  $\text{H}_2\text{O}_2$  is still needed in these efficient catalytic processes, which is uneconomical for

\* Corresponding authors at: College of Environmental Science and Engineering, Hunan University, Changsha, Hunan 410082, China.

E-mail addresses: [zgming@hnu.edu.cn](mailto:zgming@hnu.edu.cn) (G. Zeng), [laicui@hnu.edu.cn](mailto:laicui@hnu.edu.cn) (C. Lai).

<sup>1</sup> These authors contribute equally to this article.

practical application. How to solve the limitation of the advanced biomimetic hemin-contained catalysts is a challenge.

Since graphene (Nobel Prize in 2010) became the research hotspot, studies on two-dimensional (2D) nanomaterials have escalated sharply due to their excellent photoelectric properties [38–44]. 2D Bismuth tungstate (BWO), constructed by  $[\text{WO}_4]^{2-}$  -  $[\text{Bi}_2\text{O}_2]^{2+}$  -  $[\text{WO}_4]^{2-}$  layers, is one of the most promising photocatalytic materials [45,46]. The layered structure benefits the photogenerated charge-carriers separation [47–53]. Notably, compared with one-dimensional and three-dimensional structure, 2D BWO is believed to perform better photocatalytic performance: (i) charge migration distance can be reduced for the bulk to the surface [54]; (ii) the uncoordinated surface atoms in 2D structure contribute to the higher harvest of solar light [55,56]; (iii) large open and accessible surface area benefits the substrate diffusion and binding interactions [57,58], also allows higher light absorption and more oxygen vacancies generation [59–61]; (iv) 2D structure is an excellent platform for the design of novel multicomponent materials to achieve higher efficient catalytic performance [62,63].

Therefore, in this work, we used 2D BWO as the support for hemin to maintain their activity, meanwhile the introduction of hemin showed the potential to promote the photocatalytic activity of 2D BWO by improving the electronic property. Monomeric hemin was immobilized on the surface of 2D BWO to form hemin-bismuth tungstate (HBWO) composites via a facile hydrothermal method. The structure and photoelectric property were explored in detail. The photocatalytic performance of HBWO composites were investigated by the degradation of tetracycline (TC), which commonly exist in environment and are harmful for living beings. It is anticipated that the 2D nano-structured HBWO composite can be a promising biomimetic photocatalytic material for the degradation of environmental pollutants via an eco-friendly way.

## 2. Experimental

### 2.1. Synthesis of catalysts

All the reagents were analytical grade. HBWO were prepared through one-step hydrothermal process. Typically,  $\text{Bi}(\text{NO}_3)_3 \cdot 5\text{H}_2\text{O}$  was dispersed in 6.8 wt% nitrate solution to get solution A with concentration at 0.067 M, and  $\text{Na}_2\text{WO}_4 \cdot 2\text{H}_2\text{O}$  was dispersed in deionized water to get solution B (0.033 M). Then solution B was added dropwise into the solution A under stirring, mixed with 0.05 g of cetyltrimethyl ammonium bromide and a certain amount of hemin methanol solution. After magnetically stirring for 6 h and adjusting pH to 7, the mixture was transferred to Teflon-lined autoclave and sealed into a steel tank, then heated to 180 °C and maintained for 16 h. 2D HBWO was obtained. The different mass ratio of hemin/BWO at 0.5 wt%, 1.0 wt%, 3.0 wt%, 5.0 wt%, 7.0 wt% were prepared and signed as 0.5HBWO, 1HBWO, 3HBWO, 5HBWO, 7HBWO, respectively. 2D BWO was synthesized via the parallel preparation process without hemin.

### 2.2. Characterization

Crystallographic information was recorded by powder X-ray diffraction (XRD-6100, Cu  $\text{K}\alpha$  radiation,  $\lambda = 0.15418 \text{ nm}$ ). The morphology and microstructure were investigated by high resolution transmission electron microscopy (HRTEM, Tecnai G2 F20 S-TWIN) and atomic force microscopic (AFM, Bioscope system). The surface elemental compositions were identified by X-ray photoelectron spectroscopy (XPS, ESCALAB 250Xi spectrometer).

### 2.3. Photocatalytic experiments

Tetracycline (TC) was chosen as the target pollutant. The photocatalytic activities were investigated by the photodegradation of TC under simulated solar light irradiation (Xe lamp, CELHXF300). 0.2 g/L

catalyst was dispersed into 10 mg/L TC solution in the photodegradation experiment. The Xiangjiang River water, Taozi Lake water and tap water (Changsha, Hunan, China) were filtrated by a 0.22  $\mu\text{m}$  filter membrane. Before irradiation, dark reaction was performed to reach the adsorption/desorption equilibrium. Reaction solution was collected at given time interval and then filtered through 0.45  $\mu\text{m}$  membrane filters. TC concentration was analyzed by a Shimadzu UV-vis spectrophotometer with the absorbance at the characteristic band of 357 nm. The photodegradation intermediates of TC were obtained by a high-performance liquid chromatography-mass spectrometry (HPLC-MS, 1290/6460 Triple Quad). Each experiment for photocatalytic activities was performed in triplicate.

### 2.4. Optical property and photo-electrochemical measurements

Optical properties were investigated by UV-vis diffuse reflectance spectrophotometer (DRS, Hitachi U4100 UV), photoluminescence measurements (PL, FluroMax-4), and transient photocurrent response, Mott-Schottky and electrochemical impedance spectroscopy (IT, M-S and EIS, CHI760E workstation). The electron spin resonance (ESR) signals of radicals spin-trapped by 5,5-dimethyl-1-pyrroline N-oxide (DMPO) in water were performed on a Bruker ER200-SRC spectrometer. And the effect of  $\text{h}^+$ ,  $\cdot\text{O}_2^-$  and  $\cdot\text{OH}$  in TC degradation was detected by active species trapping tests. Ethylenediaminetetraacetic acid disodium salt (EDTA-2Na), tetramethylpiperidine (TEMPO) and isopropyl alcohol (IPA) were used as the scavengers for  $\text{h}^+$ ,  $\cdot\text{O}_2^-$  and  $\cdot\text{OH}$ , respectively.

## 3. Results and discussion

### 3.1. Characterizations

XRD analysis was used to record the crystal phase. As presented in Fig. 1, the distinct diffraction peaks of all the samples located at 28.3°, 32.8°, 47.1°, 56.0°, and 58.5°, corresponding to the (131), (200), (202), (133), (262) crystal planes of orthorhombic BWO (JCPDS NO. 39-0526), respectively [55]. No other crystalline phase was detected, suggesting that the introduction of hemin did not affect the crystal phase of 2D BWO. The peak intensity of HBWO composites was higher than that of 2D BWO, showing that the introduction of moderate hemin improved the crystallization. The increased peak intensity of HBWO might because the crystal nucleation centers preferred on hemin owing to the aromatic system, and then HBWO with larger particle size than

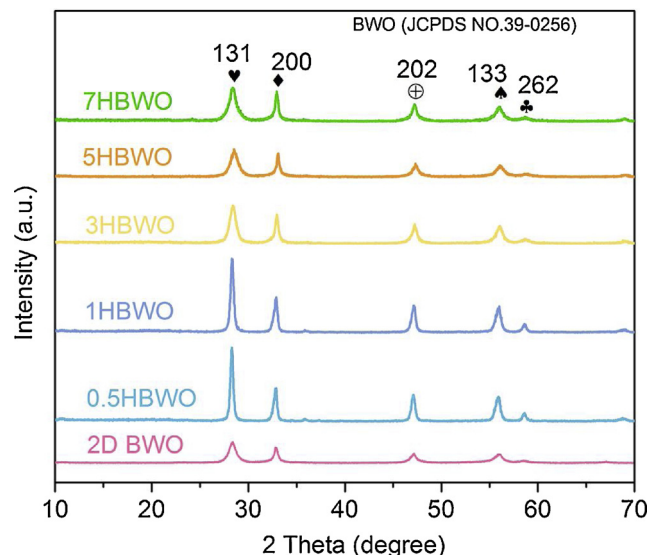
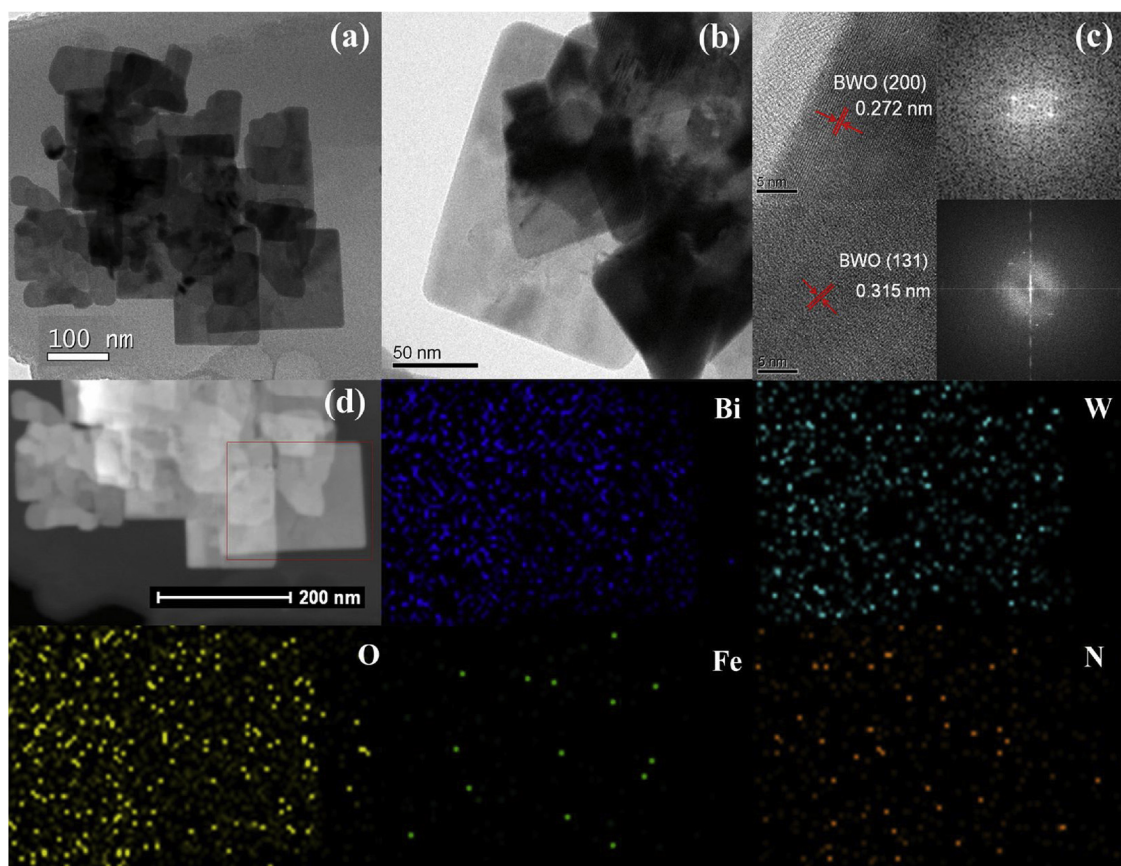


Fig. 1. XRD analysis of 2D BWO and HBWO composites.



**Fig. 2.** (a–c) TEM and HR-TEM images of 1HBWO; (d) HAADF-STEM image and the corresponding EDS elemental mapping images of 1HBWO composite.

BWO was formed (Fig. 3) [64–66]. However, the intensity of the peaks decreased with the hemin weight ratio increased, showing that excess hemin restrained the crystallization course of BWO. This because it is easier for excess hemin to form hemin aggregates, which might affect the role of aromatic system in the crystallization of HBWO [67]. Based on these results, it was preliminary concluded that optimum mass ratio of hemin/BWO was 1.0 wt%. Additionally, according to Bragg equation ( $2d\sin\theta = n\lambda$ ,  $d$  is the interplanar spacing,  $\theta$  is the Bragg angle,  $n$  is the order of the reflection, and  $\lambda$  is equal to 0.15418 nm), 0.32 nm of the interplanar spacing of 1HBWO can be obtained.

Morphology and microstructure of 1HBWO were observed by HRTEM. As shown in Fig. 2, Fig. 2 a and b exhibited the prepared 1HBWO of a regular sheet shaped structure with size of  $\sim 150 \times 250$  nm. The  $d$  spacing value of the lattice fringe, 0.272 nm and 0.315 nm, were found in Fig. 2c, corresponding to the (200) and (131) planes, respectively (Table S1). The composition of 1HBWO was further explored via high-angle annular dark-field scanning transmission electron microscopy (HAADF-STEM) and energy dispersive X-ray spectroscopy (EDS) elemental scanning. The results were presented in Fig. 2d, showing the distribution of Bi, W, O, Fe, and N elements in 1HBWO. And the homogeneous distribution of Fe and N originating from hemin can be found obviously.

Detailed size and thickness were determined by AFM, shown by the AFM images and the corresponding height histograms. As-prepared pure 2D BWO showed a size of  $\sim 180 \times 200$  nm and a thickness of 5.9 nm (Fig. 3a, b, c), while 1HBWO showed a size of  $\sim 200 \times 200$  nm and a thickness of 20.6 nm (Fig. 3d, e). Presumably, monomeric hemin with the thickness of 0.2 nm [36] was uniformly assembled on 2D BWO to form 1HBWO nanomaterials, which might show a sandwich structure built by hemin-BWO-hemin layers (Fig. 3f). We speculated that 1HBWO contained 3~4 layers with a suitable interlayer spacing. A numerical equation can be built:  $A + m(B + A) + 2m \times D = C$  ( $A$  is the thickness

of monomeric hemin,  $B$  is the thickness of BWO,  $C$  is the thickness of 1HBWO,  $D$  is the interlayer spacing,  $m$  is the number of layers).  $D$  (the interlayer spacing) is calculated to be 0.35 nm. Overall, HRTEM and AFM analysis affirmed the successful assembly of 2D nano-structured 1HBWO.

The surface elemental composition and oxidation state of 1HBWO were determined by XPS. Fig. 4a represented a survey spectrum, indicating the main peaks of Bi, W, C and O element. The 1HBWO sample showed Bi 4f and W 4f signals with a Bi/W ratio of 2.02, which is nearly equal to stoichiometric ratio of 2D BWO. High-resolution spectra of Bi 4f (Fig. 4b) at 158.4 eV and 163.8 eV (5.4 eV of doublet separation energy) corresponded to the binding energy of Bi 4f<sub>7/2</sub> and Bi 4f<sub>5/2</sub>, respectively, indicating the existence of Bi<sup>3+</sup>. Correspondingly, high resolution spectra of W 4f (Fig. 4c) at 34.9 eV and 37.1 eV (2.2 eV of /doublet separation energy) belong to the binding energy of W 4f<sub>7/2</sub> and W 4f<sub>5/2</sub> with a ratio of 4:3 in peak area, indicating the same valence state of W in +6 oxidation state. Compared with the peak of BWO, the Bi 4f peak of 1HBWO displayed a shift  $\sim 0.4$  eV and the W 4f peak showed a shift  $\sim 0.3$  eV to lower binding energies because of the interaction between hemin and BWO. The O 1s peaks at 529.8 eV and 531.6 eV (Fig. 4d) belong to the binding energy of Bi–O and O=C=O. The C 1s peak at 284.9 eV (Fig. 4e) is attributed to C–C/–CH<sub>x</sub> [68]. In the N 1s spectra (Fig. 4f), binding energy peak of C=N–C is located at 397.9 eV [69], and the peak at 402.1 eV is originating from pyridine-N [70]. XPS analysis indicates the presence of hemin and BWO in 1HBWO.

### 3.2. Photoactivity test

TC, a representative antibiotic, is widely used by many industries during the last decades. In this work, the photoactivity of HBWO composites was determined by the photocatalytic degradation of TC

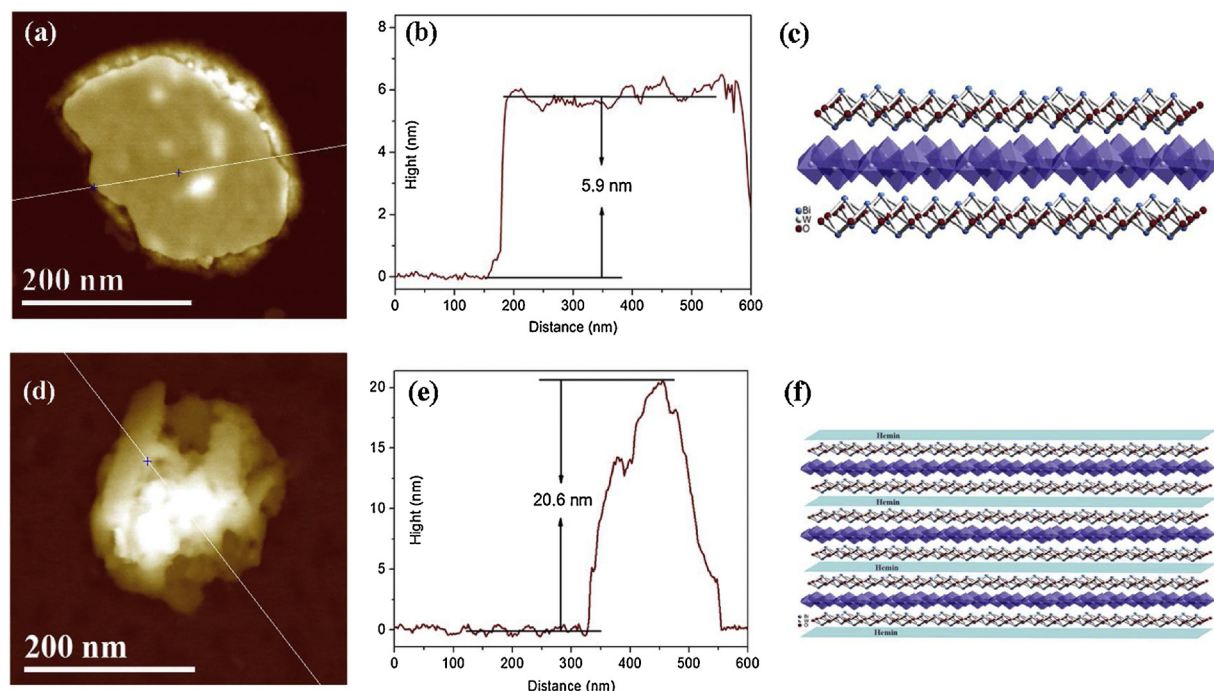


Fig. 3. (a) AFM image, (b) cross-section profile and (c) proposed structural diagram of 2D BWO; (d) AFM image, (e) cross-section profile and (f) proposed structural diagram of 1HBWO composite.

under simulated solar light irradiation, exploring the effect of different mass ratio of hemin/BWO, the effect of water matrix and the effect of inorganic salt ions. According to the dark adsorption experiment of HBWO, the absorption of TC reached absorption equilibrium within 60 min. As shown in Fig. S1, after 60 min, 4.5%, 6.3%, 6.2%, 2.4%,

4.8% and 4.2% of TC were absorbed by 2D BWO, 0.5HWBO, 1HBWO, 3HBWO, 5HBWO, and 7HBWO, respectively. The absorption experiment demonstrated that the introduction of hemin had a small impact on the absorption of TC.

Fig. 5a and b showed the photocatalytic degradation efficiency of

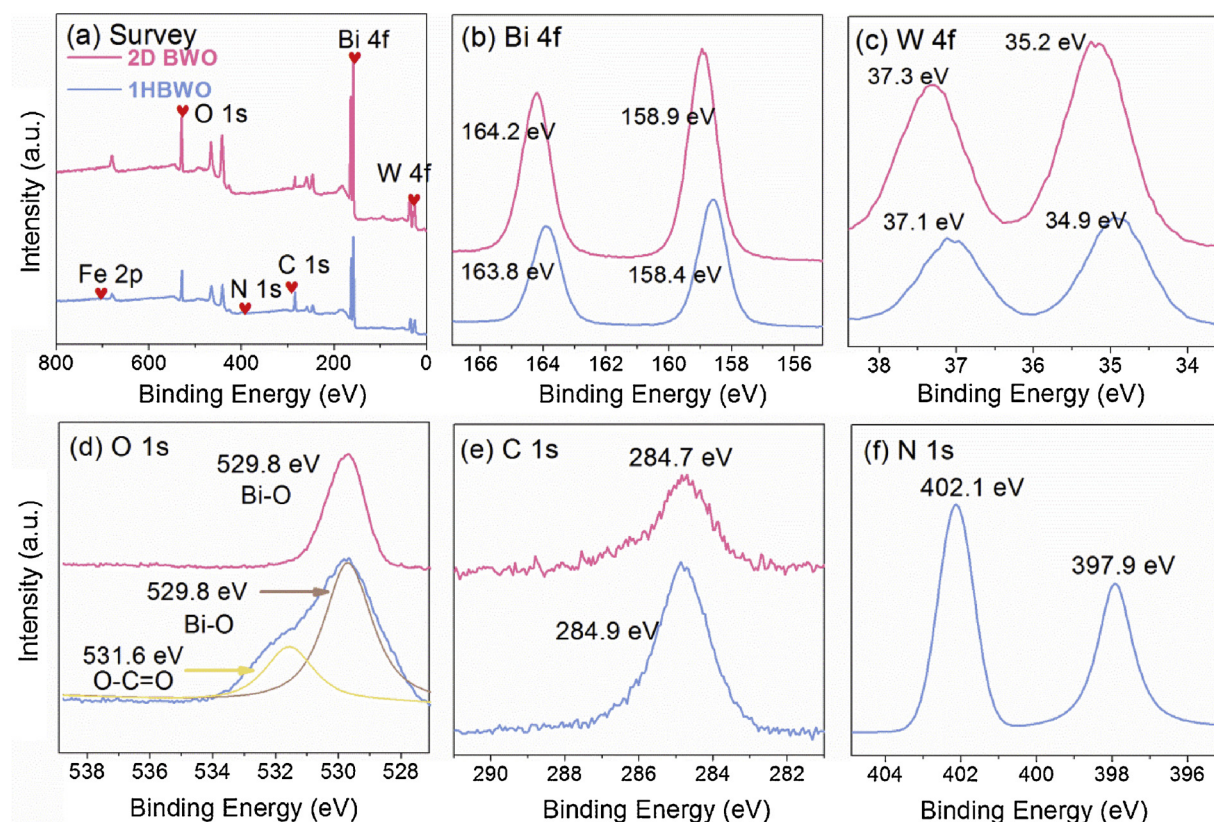


Fig. 4. XPS analysis of 2D BWO and 1HBWO composite: (a) survey spectra, (b) Bi, (c) W 4f; (d) O 1s; (e) C 1s; (f) N 1s.

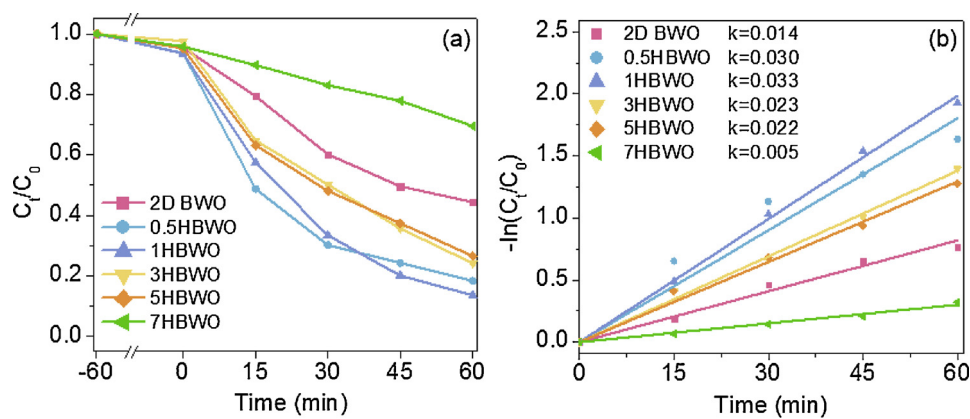


Fig. 5. (a) Photocatalytic degradation efficiency and (b) kinetics ( $k / \text{min}^{-1}$ ) of TC over 2D BWO and HBWO composites with different mass ratio of hemin/BWO.

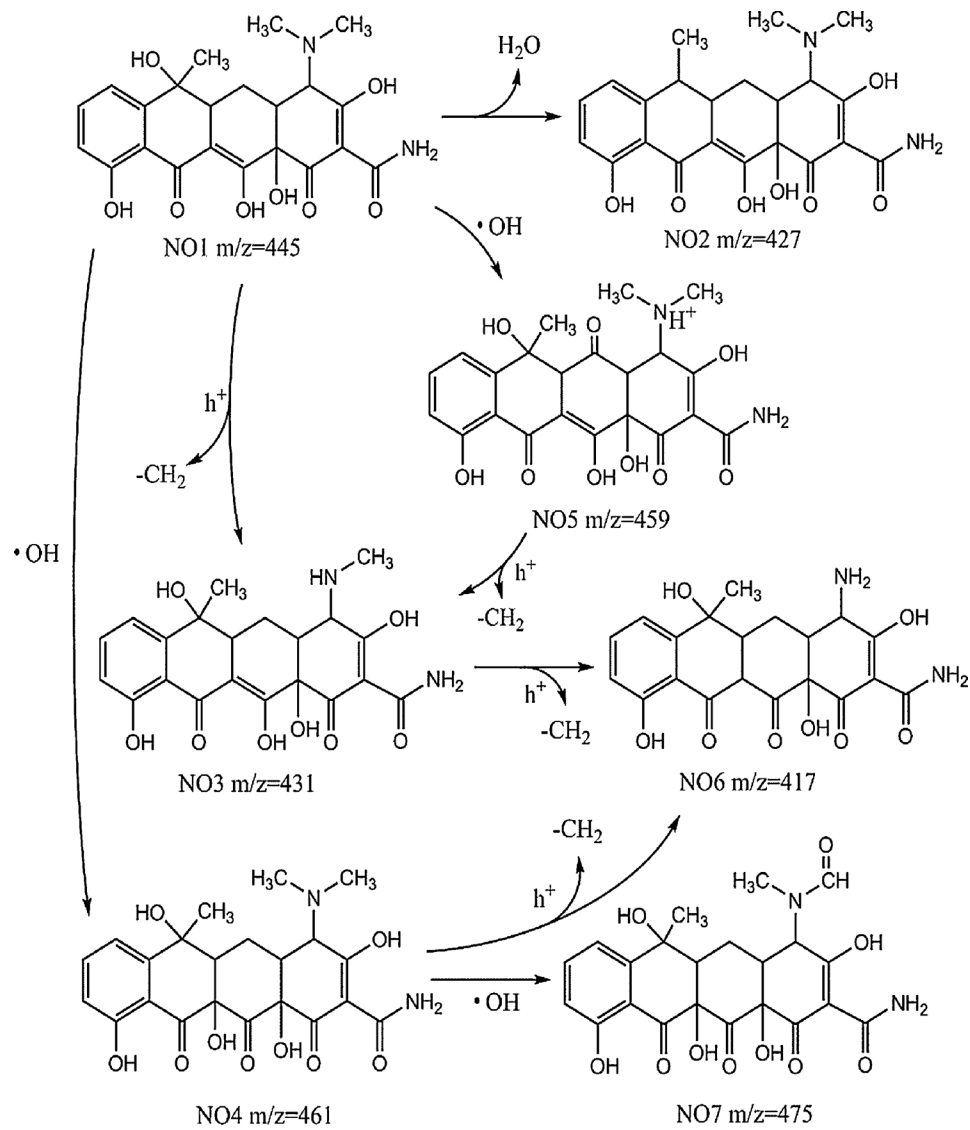
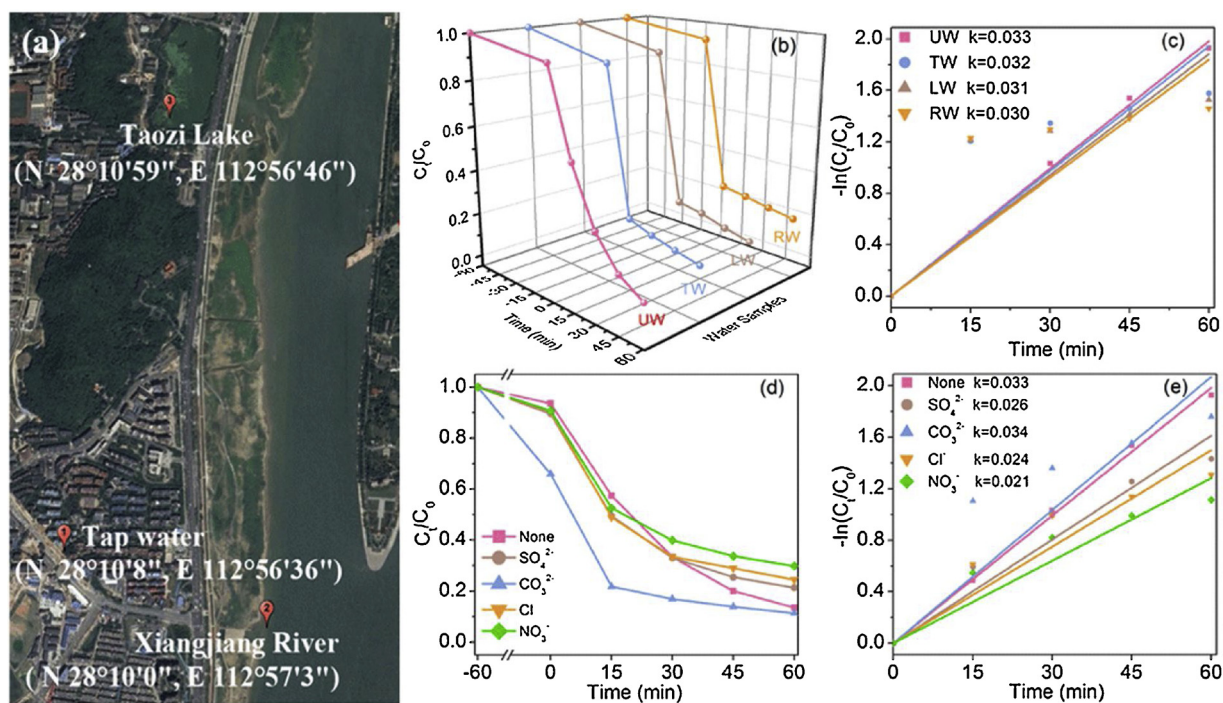


Fig. 6. Photodegradation intermediates of TC and the possible degradation processes.

TC over HBWO with different mass ratio of hemin/BWO. As shown in Fig. 5a, 55.6% TC can be photodegraded over 2D BWO after 60 min. When 0.5%–5.0% hemin was introduced, the photocatalytic performance of TC degradation was improved. The 1HBWO exhibited the highest photocatalytic efficiency, which reached 86.4%. The

photocatalytic degradation efficiency of HBWO composites decreased with increasing hemin weight ratio (when ratio  $> 1.0 \text{ wt\%}$ ). 7HBWO showed the worst photocatalytic performance on TC degradation. This might be because too much hemin immobilized on the surface of 2D BWO might shadow the reactive sites. Overall, the introduction of hemin



**Fig. 7.** (a) The sampling sites of natural water sources; (b) Photocatalytic degradation and (c) kinetics of TC over 1HBWO composite in ultrapure water (UW), tap water (TW), Lake water (LW) and River water (RW) ( $k / \text{min}^{-1}$ ); (d) Effect of coexisting inorganic salt ions on the degradation efficiency and (e) kinetics of TC over 1HBWO ( $k / \text{min}^{-1}$ ): 0.5 mM of coexisting anions in 10 mg/L TC solution.

**Table 1**

Parameters of the tap water (TW), Lake water (LW) from Taozi Lake, and River water (RW) from Xiangjiang River.

Samples	pH	$\text{Cl}^- (\text{mg L}^{-1})$	$\text{SO}_4^{2-} (\text{mg L}^{-1})$	$\text{NO}_3^- (\text{mg L}^{-1})$
TW	7.15	0.058	16.2	1.260
LW	6.91	0.074	14.3	0.872
RW	6.72	0.084	20.5	1.130

with the content range at 0.5%–5.0% can enhance the photocatalytic performance of HBWO. The photocatalytic degradation kinetics of TC was also explored, which was shown in Fig. 5b. Obviously, 1HBWO showed the highest rate constant of  $0.033 \text{ min}^{-1}$ . 1HBWO was the optimum photocatalyst, which was used in the next photocatalytic tests. And the catalytic performance of HBWO was compared with several reported biomimetic catalysts, listed in Table S2.

Additionally, the photodegradation intermediates of TC were detected by HPLC-MS. HPLC-MS spectra of the TC intermediates eluted in the photodegradation process were presented in Fig. S2 and the intermediates were listed in Table S3. It can be seen from Fig. S2 that the intensity of the peak with  $m/z$  of 445 (TC) was decreasing with the reaction time. Dehydration and hydroxylation process by  $\cdot\text{OH}$  attack and N-demethylation process (low bond energy of N–C) via  $\text{h}^+$  attack played key roles in the TC photodegradation [71,72]. The possible degradation processes were presented in Fig. 6. Intermediate  $\text{NO}_2$  was generated via the dehydration process.  $\cdot\text{OH}$  can directly attack the TC molecules in the hydroxylation process to produce intermediate  $\text{NO}_4$

and  $\text{NO}_5$ , and then  $\text{NO}_4$  can be degraded to  $\text{NO}_7$ . Intermediate  $\text{NO}_5$  was formed mainly via the N-demethylation process of TC and  $\text{NO}_5$ . Additionally, intermediate  $\text{NO}_6$  can be produced from the N-demethylation of  $\text{NO}_3$  and  $\text{NO}_4$ . Overall, these detected intermediates confirmed that TC was degraded progressively via the photocatalytic process over HBWO.

In practical application, water matrix is a crucial factor. In this work, ultrapure water (UW), tap water (TW), Lake water (LW) and River water (RW) were used to investigate the effect of water matrix on the photocatalytic degradation of TC over 1HBWO. The sampling sites were shown in Fig. 7a. After 60 min irradiation, photocatalytic efficiency of TC degradation achieved 86.4%, 81.4%, 80.2%, and 78.1% (Fig. 7b), and the rate constant was  $0.033 \text{ min}^{-1}$ ,  $0.032 \text{ min}^{-1}$ ,  $0.031 \text{ min}^{-1}$ , and  $0.030 \text{ min}^{-1}$  (Fig. 7c) in TC-obtained UW, TW, LW, and RW, respectively. According to the detected parameters of the water sources (Table 1), the pH value increased in the order as follows: RW < LW < TW. Based on the experimental results, presumably a slight higher pH range at 6.0–7.5 had a positive effect on the photocatalytic degradation of TC over 2D 1HBWO in natural water. This positive effect might be ascribed to the surface charge variations of TC adsorbed onto the surface of catalysts [73]. Photodegradation of TC over 1HBWO composite maintained high efficiency in real water matrix.

Besides, the effect of inorganic salt ions (including  $\text{CO}_3^{2-}$ ,  $\text{Cl}^-$ ,  $\text{SO}_4^{2-}$  and  $\text{NO}_3^-$ ) was investigated, because the electrolytes might have an effect on the photocatalytic activity. As shown in Fig. 7d and e,  $\text{Cl}^-$ ,  $\text{SO}_4^{2-}$  and  $\text{NO}_3^-$  had a little negative effect on the photocatalytic

**Table 2**

Zeta potentials and pH of the TC solution in the presence of HBWO with different inorganic salt ions.

Inorganic salt ions	None	$\text{CO}_3^{2-}$	$\text{Cl}^-$	$\text{SO}_4^{2-}$	$\text{NO}_3^-$
Zeta potential (mV)	$-29.8 \pm 1.5$	$-31.9 \pm 0.8$	$-10.2 \pm 1.7$	$-23.6 \pm 1.8$	$-17.8 \pm 0.9$
pH	5.68	9.64	6.10	5.97	5.95

<sup>a</sup>Experimental conditions:  $m/v = 0.2 \text{ g/L}$ , TC (100 ml, 10 mg/L), and inorganic salt ions concentration (0.5 mM).

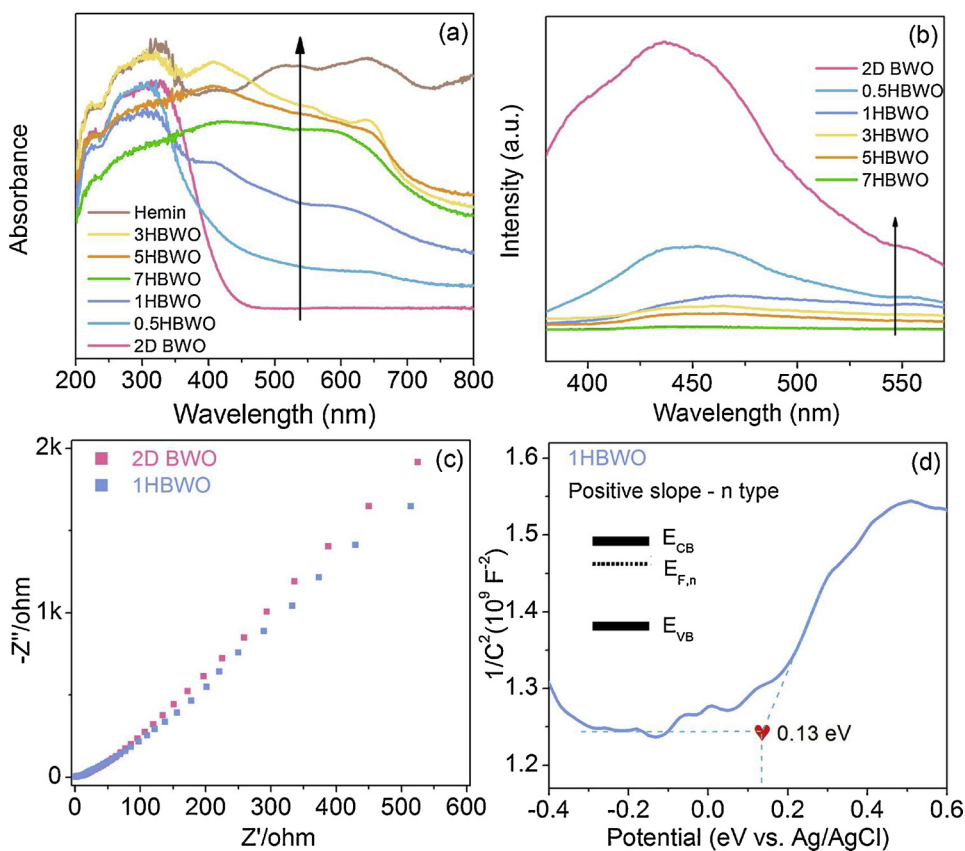


**Fig. 8.** Optical property analysis: (a) DRS of the prepared catalysts, (b) PL of the prepared catalysts, and (c) EIS of 2D BWO and 1HBWO; (d) M-S analysis of 1HBWO film electrode in 0.5 M of  $\text{Na}_2\text{SO}_4$  solution with pH located at 5.96.

efficiency of TC degradation over 1HBWO composite with the solution pH at about 6.0. The negative effect can be listed as the following decreasing order:  $\text{NO}_3^- > \text{Cl}^- > \text{SO}_4^{2-}$ . According to the Zeta potentials of the TC solution (Table 2), the Zeta potentials of  $\text{Cl}^-$ -TC solution,  $\text{SO}_4^{2-}$ -TC solution and  $\text{NO}_3^-$ -TC solution were more positive than that of the condition ( $-29.8 \pm 1.5$ ), showing that TC adsorption on the catalysts might be inhibited. The decrease in the photocatalytic efficiency might attribute to the enhanced electrostatic repulsion and the competitive adsorption between the inorganic ions and TC for the limited active sites on the catalysts [74]. The Zeta potential of  $\text{SO}_4^{2-}$ -TC solution ( $-23.6 \pm 1.8$ ) was closest to that of the condition ( $-29.8 \pm 1.5$ ), contributing to the lowest negative effect caused by  $\text{SO}_4^{2-}$ .  $\text{NO}_3^-$  showed photoabsorption at the solar light ranging from 290 to 370 nm, leading to the light-filtering effects, which negatively affected the photodegradation efficiency [75]. This might be the reason why  $\text{NO}_3^-$  showed higher negative effect than  $\text{Cl}^-$ . On the contrary,  $\text{CO}_3^{2-}$  slightly facilitated the photocatalytic degradation of TC over 1HBWO composite. This might be ascribed to the enhanced adsorption of TC on catalysts owing to the more negative Zeta potential ( $-31.9 \pm 0.8$ ) and higher pH value (9.64) caused by the generation of  $\text{OH}^-$  [73]. Overall, the results demonstrated that the photocatalytic process over 1HBWO composite was an efficient technology for TC removal in practical application.

### 3.3. Photocatalytic mechanism

#### 3.3.1. Optical property

The optical property of pure 2D BWO and HBWO composites were investigated by UV-vis DRS, which were shown in Fig. 8a. It can be found that pure 2D BWO exhibits the absorption of light shorter than 450 nm, and HBWO composites show enhanced optical absorption in the range 450–800 nm. Hemin showed the highest absorption of light

owing to the blackbody nature. This phenomenon suggested that HBWO composite might possess higher photoactivity, and hemin played an important role in the enhanced photoabsorption. Fig. 8b showed steady-state PL spectra of as-prepared photocatalysts, which indicated the behavior of photogenerated charge carriers [76]. It can be found that the emission peak centered at around 450 nm, and HBWO composites showed a lower intensity of centered peak, indicating the reduced recombination of photoelectrons and holes. However, introduction of too much hemin, like 7HBWO, might form inactive hemin aggregates and shadow the surface active sites of 2D BWO photocatalysts, and then reduce the generation of charge carriers. The introduction of hemin in moderation can not only enhance the utilization of wider spectrum light irradiation, also boost the separation of photogenerated electrons and holes, thus improving the photocatalytic performance.

In order to further prove this assumption, EIS and IT were performed under light irradiation. From the EIS Nyquist plot (Fig. 8c), it can be found that the arc radius of the ITO/1HBWO film was lower than that of the ITO/2D BWO film, exhibiting a higher efficiency of electron transfer at the electrodes. The electron-transfer efficiency is affected by the corresponding charge transport behavior [77]. The photogenerated electrons were reduced by the oxygen carried by HBWO, accelerating the charge carriers transfer and then showing a higher electron-transfer efficiency. According to the IT result (Fig. S3), 1HBWO showed the increased transient photocurrent than 2D BWO, indicating the improved separation of electrons and holes.

Fig. 8d showed M-S plot of 1HBWO, which showed a positive slope, indicating the behavior of *n*-type semiconductor [78]. So the introduction of hemin did not change the *n*-type behavior of 2D BWO. In *n*-type semiconductor, the bottom of the conduction band (CB) is more negative (about 0.2 eV) than Fermi level. Besides, M-S analysis can be used to determine the flat band potential via extrapolating to the

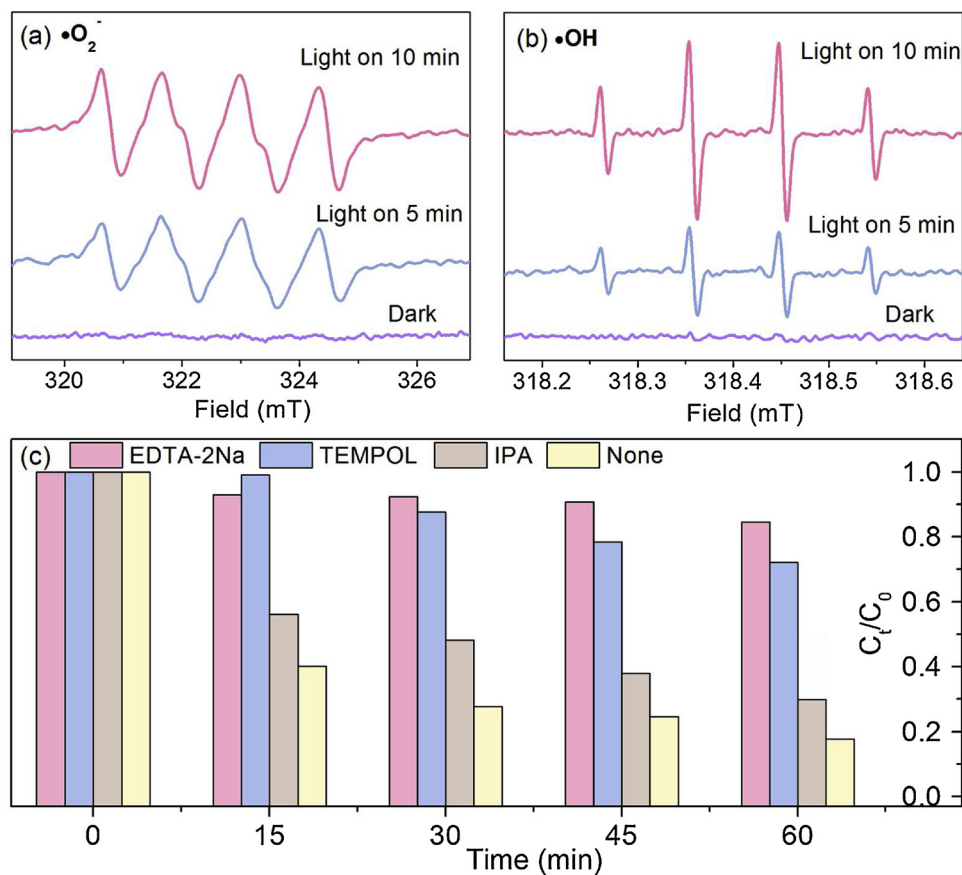


Fig. 9. ESR spectra of (a) DMPO-·O<sub>2</sub><sup>-</sup> adduct in methanol dispersion and (b) DMPO-·OH adduct in aqueous dispersion for 1HBWO; (c) scavenger tests: 2 mmol scavengers in 100 mL 10 mg/L TC solution.

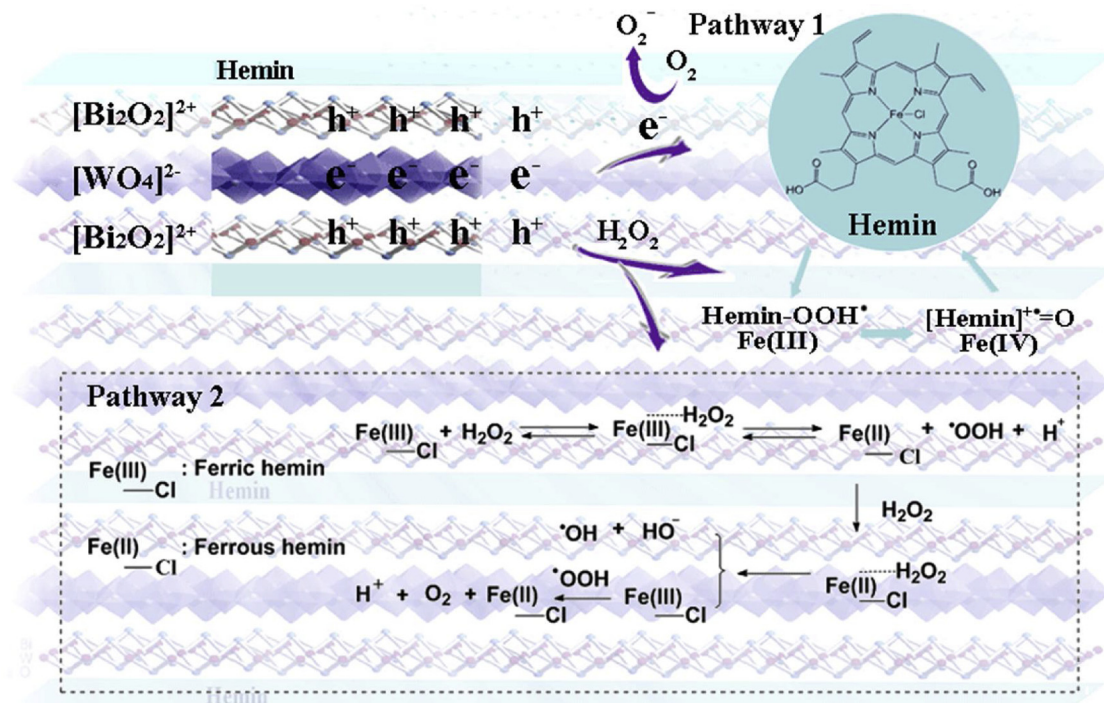


Fig. 10. Possible photocatalytic reaction mechanism over HBWO composites under solar irradiation.

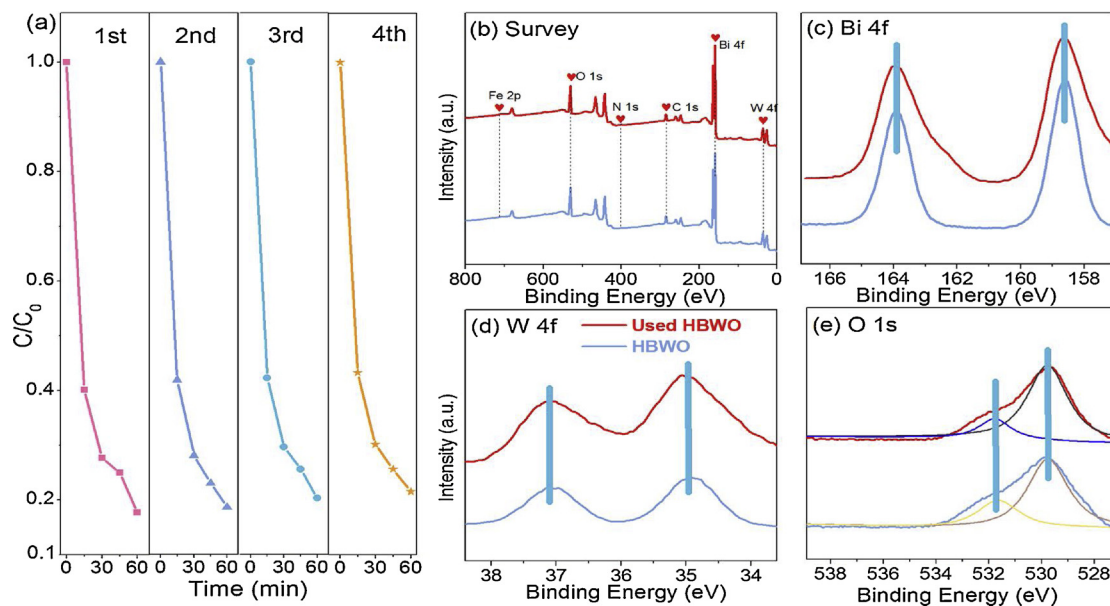


Fig. 11. (a) Cycling runs of TC photodegradation over 1HBWO; XPS analysis of fresh and Used 1HBWO: (b) survey spectra, (c) Bi, (d) W 4f; (e) O 1s.

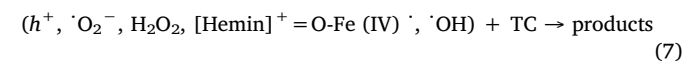
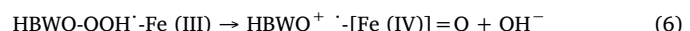
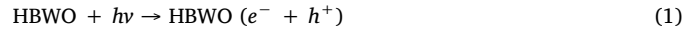
intercept of the x-axis. The flat band potential was inferred to be around +0.13 eV vs. Ag/AgCl. And generally, the Fermi level is equal to the flat band potential. Therefore, the  $E_{CB}$  of HBWO can be inferred to be around +0.13 eV vs. NHE, which is more negative than  $E^0(O_2/H_2O_2)$  (+0.682 V vs. NHE).

### 3.3.2. Roles of radical species

To investigate the presence of radical species in the degradation of TC over HBWO composite, ESR was conducted. As shown in Fig. 9a and b, both  $\cdot OH$  and  $\cdot O_2^-$  radicals signal were observed after irradiation, suggesting the generation of  $\cdot OH$  and  $\cdot O_2^-$  radicals during the photocatalytic process, which can improve the photocatalytic performance of HBWO composite. After that, scavenger tests were performed to study the roles of active radical species in TC photodegradation. Fig. 9c showed that the photocatalytic efficiency of TC degradation was inhibited greatly when EDTA-2Na and TEMPOL was added, suggesting that holes and  $\cdot O_2^-$  played the main roles in the catalytic process. The degradation efficiency decreased slightly when adding IPA, suggesting that just a small amount of  $\cdot OH$  radicals participated in photocatalytic degradation of TC. The ESR analysis and scavenger tests indicated that photogenerated holes and  $\cdot O_2^-$  were the main active species in the photocatalytic degradation of TC. Additionally, maximum 36  $\mu\text{mol/L}$  of  $H_2O_2$  was generated in the photocatalytic process, measured via UV-vis spectrophotometer after complexation with metavanadate [79].

### 3.3.3. Mechanism of the improved photocatalytic activity

Based on the above results, the improved photocatalytic performance of HBWO composites can be explained as follows (Fig. 10): (i) the introduction of moderate hemin in HBWO can enhance the utilization of wider spectrum of light owing to the blackbody nature; (ii) 2D structure benefited the faster transfer of photogenerated charge carriers, and the uncoordinated surface atoms in the 2D structure can improve the harvest of solar light; (iii) hemin played as an electron shuttle to transfer the electrons in CB of HBWO, thus enhanced the separation efficiency of electrons and holes. The holes left in VB can oxidize TC directly; (iv) hemin is an oxygen transfer reagent, and the oxygen molecules carried by hemin can combined with the electrons on CB of HBWO to form  $\cdot O_2^-$ , leading to the degradation of TC; (v)  $H_2O_2$  generated in the photocatalytic process can induce the Fenton-like reaction (two possible pathways) with high oxidizing capacity [37,80]. The photocatalytic degradation process can be described as follows:



### 3.3.4. Stability of synthesized catalyst

The recyclability and physicochemical stability of HBWO in TC photodegradation was explored in detail. 1HBWO was performed four reaction runs, and the results of the cyclic experiments were shown in Fig. 11a. Obviously, a high TC photodegradation efficiency of 78.5% can be still obtained over 1HBWO after four cycles. Besides, XPS spectra of the fresh and used 1HBWO were shown in Fig. 11(b–e), including the survey spectra, Bi 4f, W 4f and O1s. It was found that the chemical composites and valence state of 1HBWO kept unchanged after the photodegradation reaction. Moreover, FTIR and SEM of the used 1HBWO were detected to further demonstrate the stability (Figs. S4 and S5). No apparent changes were observed. These results affirmed the stability of the synthesized HBWO photocatalysts in the TC photodegradation process.

## 4. Conclusion

In summary, HBWO composites with 2D structure were successfully synthesized via a one-step hydrothermal process. Based on the characterization analysis of the structure, morphology and photoelectric property, the composite was formed with hemin immobilized on the surface of 2D BWO. And the synthesized HBWO showed layered structure with the interlayer spacing at ~0.35 nm. HBWO with mass ratio of hemin/BWO ranging at 0.5%–5.0% exhibited improved photocatalytic performance for TC degradation under irradiation. The excellent photocatalytic performance was attributed to the enhanced photoabsorption and faster electron and oxygen transfer. According to the ESR analysis and scavenger tests, holes and  $\cdot O_2^-$  played the main

roles in the photocatalytic degradation of TC. It should be noted that the synthesized HBWO shows high catalytic performance in the environmental pollutant degradation, which can well meet the requirement of green development.

## Acknowledgements

This study was financially supported by the Program for the National Natural Science Foundation of China (51879101, 51579098, 51779090, 51709101, 51521006, 51809090, 51278176, 51378190), the National Program for Support of Top-Notch Young Professionals of China (2014), the Program for Changjiang Scholars and Innovative Research Team in University (IRT-13R17), and Hunan Provincial Science and Technology Plan Project (2018SK20410, 2017SK2243, 2016RS3026), and the Fundamental Research Funds for the Central Universities (531109200027, 531107051080, 531107050978).

## Appendix A. Supplementary data

Supplementary material related to this article can be found, in the online version, at doi:<https://doi.org/10.1016/j.apcatb.2019.03.008>.

## References

- [1] K. Chen, X.Y. Huang, S.B.J. Kan, R.K. Zhang, F.H. Arnold, Enzymatic construction of highly strained carbocycles, *Science* 360 (2018) 71–75.
- [2] L.Y. Zhang, M. Can, S.W. Ragsdale, F.A. Armstrong, Fast and selective photo-reduction of CO<sub>2</sub> to CO catalyzed by a complex of carbon monoxide dehydrogenase, TiO<sub>2</sub>, and Ag nanoclusters, *ACS Catal.* 8 (2018) 2789–2795.
- [3] T. Xu, D. Wang, L. Dong, H. Shen, W. Lu, W. Chen, Graphitic carbon nitride co-modified by zinc phthalocyanine and graphene quantum dots for the efficient photocatalytic degradation of refractory contaminants, *Appl. Catal. B: Environ.* 244 (2019) 96–106.
- [4] H.P. Cheng, M.C. Hu, Q.G. Zhai, S.N. Li, Y.C. Jiang, Polydopamine tethered CPO/HRP-TiO<sub>2</sub> nano-composites with high bio-catalytic activity, stability and reusability: enzyme-photo bifunctional synergistic catalysis in water treatment, *Chem. Eng. J.* 347 (2018) 703–710.
- [5] B. Biswas, B. Sarkar, R. Rusmin, R. Naidu, Bioremediation of PAHs and VOCs: advances in clay mineral-microbial interaction, *Environ. Int.* 85 (2015) 168–181.
- [6] L. Zhang, J. Zhang, G. Zeng, H. Dong, Y. Chen, C. Huang, Y. Zhu, R. Xu, Y. Cheng, K. Hou, W. Cao, W. Fang, Multivariate relationships between microbial communities and environmental variables during co-composting of sewage sludge and agricultural waste in the presence of PVP-AgNPs, *Bioresour. Technol.* 261 (2018) 10–18.
- [7] Y. Wang, Y. Zhu, Y. Hu, G. Zeng, Y. Zhang, C. Zhang, C. Feng, How to construct DNA hydrogels for environmental applications: advanced water treatment and environmental analysis, *Small* 14 (2018).
- [8] X. Tang, G. Zeng, C. Fan, M. Zhou, L. Tang, J. Zhu, J. Wan, D. Huang, M. Chen, P. Xu, C. Zhang, Y. Lu, W. Xiong, Chromosomal expression of CadR on *Pseudomonas aeruginosa* for the removal of Cd(II) from aqueous solutions, *Sci. Total Environ.* 636 (2018) 1355–1361.
- [9] X. Ren, G. Zeng, L. Tang, J. Wang, J. Wan, Y. Liu, J. Yu, H. Yi, S. Ye, R. Deng, Sorption, transport and biodegradation – an insight into bioavailability of persistent organic pollutants in soil, *Sci. Total Environ.* 610 (2018) 1154–1163.
- [10] C. Lai, X. Liu, L. Qin, C. Zhang, G. Zeng, D. Huang, M. Cheng, P. Xu, H. Yi, D. Huang, Chitosan-wrapped gold nanoparticles for hydrogen-bonding recognition and colorimetric determination of the antibiotic kanamycin, *Microchim. Acta* 184 (2017) 2097–2105.
- [11] Y. Lin, J. Ren, X. Qu, Catalytically active nanomaterials: a promising candidate for artificial enzymes, *Acc. Chem. Res.* 47 (2014) 1097–1105.
- [12] X. Ren, G. Zeng, L. Tang, J. Wang, J. Wan, H. Feng, B. Song, C. Huang, X. Tang, Effect of exogenous carbonaceous materials on the bioavailability of organic pollutants and their ecological risks, *Soil Biol. Biochem.* 116 (2018) 70–81.
- [13] Z. Huang, K. He, Z. Song, G. Zeng, A. Chen, L. Yuan, H. Li, L. Hu, Z. Guo, G. Chen, Antioxidative response of *Phanerochaete chrysosporium* against silver nanoparticle-induced toxicity and its potential mechanism, *Chemosphere* 211 (2018) 573–583.
- [14] S. Ye, G. Zeng, H. Wu, C. Zhang, J. Liang, J. Dai, Z. Liu, W. Xiong, J. Wan, P. Xu, M. Cheng, Co-occurrence and interactions of pollutants, and their impacts on soil remediation—a review, *Crit. Rev. Environ. Sci. Technol.* 47 (2017) 1528–1553.
- [15] L. Qin, G.M. Zeng, C. Lai, D.L. Huang, P.A. Xu, C. Zhang, M. Cheng, X.G. Liu, S.Y. Liu, B.S. Li, H. Yi, "Gold rush" in modern science: fabrication strategies and typical advanced applications of gold nanoparticles in sensing, *Coord. Chem. Rev.* 359 (2018) 1–31.
- [16] X. Guo, Z. Peng, D. Huang, P. Xu, G. Zeng, S. Zhou, X. Gong, M. Cheng, R. Deng, H. Yi, H. Luo, X. Yan, T. Li, Biotransformation of cadmium-sulfamethazine combined pollutant in aqueous environments: *Phanerochaete chrysosporium* bring cautious optimism, *Chem. Eng. J.* 347 (2018) 74–83.
- [17] F. He, L. Mi, Y. Shen, T. Mori, S. Liu, Y. Zhang, Fe–N–C artificial enzyme: activation of oxygen for dehydrogenation and monooxygenation of organic substrates under mild condition and cancer therapeutic application, *ACS Appl. Mater. Interfaces* 10 (2018) 35327–35333.
- [18] S. Wang, H. Jiang, L. Zhang, J. Jiang, M. Liu, Enantioselective activity of hemin in supramolecular gels formed by co-assembly with a chiral gelator, *ChemPlusChem* 83 (2018) 1038–1043.
- [19] H. Wang, P. Li, D. Yu, Y. Zhang, Z. Wang, C. Liu, H. Qiu, Z. Liu, J. Ren, X. Qu, Unraveling the enzymatic activity of oxygenated carbon nanotubes and their application in the treatment of bacterial infections, *Nano Lett.* 18 (2018) 3344–3351.
- [20] L. Villarino, K.E. Splan, E. Reddem, L. Alonso-Cotchico, C.G. de Souza, A. Lledos, J.D. Marechal, A. Thunnissen, G. Roelfes, An artificial heme enzyme for cyclopropanation reactions, *Angew. Chem. Int. Ed.* 57 (2018) 7785–7789.
- [21] Z. Cai, J. Shi, Y. Wu, Y. Zhang, S. Zhang, Z. Jiang, Chloroplast-inspired artificial photosynthetic capsules for efficient and sustainable enzymatic hydrogenation, *ACS Sustain. Chem. Eng.* 6 (2018) 17114–17123.
- [22] L. Cheng, K. Yan, J.D. Zhang, Integration of graphene-hemin hybrid materials in an electroenzymatic system for degradation of diclofenac, *Electrochim. Acta* 190 (2016) 980–987.
- [23] L. Zhang, J. Zhou, F. Ma, Q. Wang, H. Xu, H. Ju, J. Lei, Single-sided competitive axial coordination of G-quadruplex/hemin as molecular switch for imaging intracellular nitric oxide, *Chem. Eur. J.* 25 (2019) 490–494.
- [24] Z. Han, J. Li, X. Han, X. Zhao, X. Ji, A novel biomimetic catalyst constructed by axial coordination of hemin with PAN fiber for efficient degradation of organic dyes, *J. Mater. Sci.* 53 (2018) 4118–4131.
- [25] S. Shao, V. Rajendiran, J.F. Lovell, Metalloporphyrin nanoparticles: Coordinating diverse theranostic functions, *Coord. Chem. Rev.* 379 (2019) 99–120.
- [26] Z. Feng, J. Yu, J. Kong, T. Wang, A novel porous Al<sub>2</sub>O<sub>3</sub> layer/AgNPs-hemin composite for degradation of azo dyes under visible and UV irradiation, *Chem. Eng. J.* 294 (2016) 236–245.
- [27] X.F. Xu, C. Li, M.T. Xiong, Z.H. Tao, Y.J. Pan, Hemin-catalyzed sulfonyl ylide formation and subsequently reactant-controlled chemoselective rearrangements, *Chem. Commun.* 53 (2017) 6219–6222.
- [28] H.T.N. Le, H.K. Jeong, Electrochemical supramolecular recognition of hemin–carbon composites, *Chem. Phys. Lett.* 698 (2018) 102–109.
- [29] B. Jiang, Y. Yao, R. Xie, D. Dai, W. Lu, W. Chen, L. Zhang, Enhanced generation of reactive oxygen species for efficient pollutant elimination catalyzed by hemin based on persistent free radicals, *Appl. Catal. B: Environ.* 183 (2016) 291–297.
- [30] Z. Li, B. Tian, W. Zhen, Y. Wu, G. Lu, Inhibition of hydrogen and oxygen recombination using oxygen transfer reagent hemin chloride in Pt/TiO<sub>2</sub> dispersion for photocatalytic hydrogen generation, *Appl. Catal. B: Environ.* 203 (2017) 408–415.
- [31] R. Qu, L. Shen, Z. Chai, C. Jing, Y. Zhang, Y. An, L. Shi, Hemin-block copolymer micelle as an artificial peroxidase and its applications in chromogenic detection and biocatalysis, *ACS Appl. Mater. Interfaces* 6 (2014) 19207–19216.
- [32] R. Wang, D. Huang, Y. Liu, C. Zhang, C. Lai, G. Zeng, M. Cheng, X. Gong, J. Wan, H. Luo, Investigating the adsorption behavior and the relative distribution of Cd<sup>2+</sup> sorption mechanisms on biochars by different feedstock, *Bioresour. Technol.* 261 (2018) 265–271.
- [33] W. Xue, D. Huang, G. Zeng, J. Wan, C. Zhang, R. Xu, M. Cheng, R. Deng, Nanoscale zero-valent iron coated with rhamnolipid as an effective stabilizer for immobilization of Cd and Pb in river sediments, *J. Hazard. Mater.* 341 (2018) 381–389.
- [34] D. Huang, C. Hu, G. Zeng, M. Cheng, P. Xu, X. Gong, R. Wang, W. Xue, Combination of Fenton processes and biotreatment for wastewater treatment and soil remediation, *Sci. Total Environ.* 574 (2017) 1599–1610.
- [35] F. Wu, H. Huang, T. Xu, W. Lu, N. Li, W. Chen, Visible-light-assisted peroxymonosulfate activation and mechanism for the degradation of pharmaceuticals over pyridyl-functionalized graphitic carbon nitride coordinated with iron phthalocyanine, *Appl. Catal. B: Environ.* 218 (2017) 230–239.
- [36] T. Xue, S. Jiang, Y. Qu, Q. Su, R. Cheng, S. Dubin, C.-Y. Chiu, R. Kaner, Y. Huang, X. Duan, Graphene-supported hemin as a highly active biomimetic oxidation catalyst, *Angew. Chem. Int. Ed.* 51 (2012) 3822–3825.
- [37] X. Chen, W. Lu, T. Xu, N. Li, D. Qin, Z. Zhu, G. Wang, W. Chen, A bio-inspired strategy to enhance the photocatalytic performance of g-C<sub>3</sub>N<sub>4</sub> under solar irradiation by axial coordination with hemin, *Appl. Catal. B: Environ.* 201 (2017) 518–526.
- [38] H. Yi, D. Huang, L. Qin, G. Zeng, C. Lai, M. Cheng, S. Ye, B. Song, X. Ren, X. Guo, Selective prepared carbon nanomaterials for advanced photocatalytic application in environmental pollutant treatment and hydrogen production, *Appl. Catal. B: Environ.* 239 (2018) 408–424.
- [39] J.L. Gong, B. Wang, G.M. Zeng, C.P. Yang, C.G. Niu, Q.Y. Niu, W.J. Zhou, Y. Liang, Removal of cationic dyes from aqueous solution using magnetic multi-wall carbon nanotube nanocomposite as adsorbent, *J. Hazard. Mater.* 164 (2009) 1517–1522.
- [40] K. He, Z. Zeng, A. Chen, G. Zeng, R. Xiao, P. Xu, Z. Huang, J. Shi, L. Hu, G. Chen, Advancement of Ag-graphene based nanocomposites: an overview of synthesis and its applications, *Small* 14 (2018) e1800871.
- [41] W. Xiong, Z. Zeng, X. Li, G. Zeng, R. Xiao, Z. Yang, Y. Zhou, C. Zhang, M. Cheng, L. Hu, C. Zhou, L. Qin, R. Xu, Y. Zhang, Multi-walled carbon nanotube/amino-functionalized MIL-53(Fe) composites: remarkable adsorptive removal of antibiotics from aqueous solutions, *Chemosphere* 210 (2018) 1061–1069.
- [42] H. Yi, G. Zeng, C. Lai, D. Huang, L. Tang, J. Gong, M. Chen, P. Xu, H. Wang, M. Cheng, C. Zhang, W. Xiong, Environment-friendly fullerene separation methods, *Chem. Eng. J.* 330 (2017) 134–145.
- [43] L. Qin, D. Huang, P. Xu, G. Zeng, C. Lai, Y. Fu, H. Yi, B. Li, C. Zhang, M. Cheng, C. Zhou, X. Wen, In-situ deposition of gold nanoparticles onto polydopamine-decorated g-C<sub>3</sub>N<sub>4</sub> for highly efficient reduction of nitroaromatics in environmental water purification, *J. Colloid Interface Sci.* 534 (2019) 357–369.

[44] P. Wei, D. Qin, J. Chen, Y. Li, M. Wen, Y. Ji, G. Li, T. An, Photocatalytic ozonation mechanism of gaseous n-hexane on  $\text{MO}_x\text{-TiO}_2$ -foam nickel composite ( $\text{M} = \text{Cu, Mn, Ag}$ ): Unveiling the role of  $\cdot\text{OH}$  and  $\cdot\text{O}_2^-$ , *Environ. Sci. Nano* (2019), <https://doi.org/10.1039/C8EN01291A>.

[45] H. Yi, L. Qin, D. Huang, G. Zeng, C. Lai, X. Liu, B. Li, H. Wang, C. Zhou, F. Huang, S. Liu, X. Guo, Nano-structured bismuth tungstate with controlled morphology: Fabrication, modification, environmental application and mechanism insight, *Chem. Eng. J.* 358 (2019) 480–496.

[46] Y.Y. Wang, W.J. Jiang, W.J. Luo, X.J. Chen, Y.F. Zhu, Ultrathin nanosheets  $\text{g-C}_3\text{N}_4@\text{Bi}_2\text{WO}_6$  core-shell structure via low temperature reassembled strategy to promote photocatalytic activity, *Appl. Catal. B: Environ.* 237 (2018) 633–640.

[47] L. Yuan, K.Q. Lu, F. Zhang, X.Z. Fu, Y.J. Xu, Unveiling the interplay between light-driven  $\text{CO}_2$  photocatalytic reduction and carbonaceous residues decomposition: a case study of  $\text{Bi}_2\text{WO}_6\text{-TiO}_2$  binanosheets, *Appl. Catal. B: Environ.* 237 (2018) 424–431.

[48] B. Li, C. Lai, G. Zeng, L. Qin, H. Yi, D. Huang, C. Zhou, X. Liu, M. Cheng, P. Xu, C. Zhang, F. Huang, S. Liu, Facile hydrothermal synthesis of Z-scheme  $\text{Bi}_2\text{Fe}_4\text{O}_9/\text{Bi}_2\text{WO}_6$  heterojunction photocatalyst with enhanced visible-light photocatalytic activity, *ACS Appl. Mater. Interfaces* 10 (2018) 18824–18836.

[49] X. Zhou, C. Lai, D. Huang, G. Zeng, L. Chen, L. Qin, P. Xu, M. Cheng, C. Huang, C. Zhang, C. Zhou, Preparation of water-compatible molecularly imprinted thiol-functionalized activated titanium dioxide: selective adsorption and efficient photodegradation of 2, 4-dinitrophenol in aqueous solution, *J. Hazard. Mater.* 346 (2018) 113–123.

[50] Y. Yang, C. Zhang, C. Lai, G. Zeng, D. Huang, M. Cheng, J. Wang, F. Chen, C. Zhou, W. Xiong, BiOX ( $\text{X} = \text{Cl, Br, I}$ ) photocatalytic nanomaterials: applications for fuels and environmental management, *Adv. Colloid Interface Sci.* 254 (2018) 76–93.

[51] C. Zhou, C. Lai, C. Zhang, G. Zeng, D. Huang, M. Cheng, L. Hu, W. Xiong, M. Chen, J. Wang, Y. Yang, L. Jiang, Semiconductor/boron nitride composites: synthesis, properties, and photocatalysis applications, *Appl. Catal. B: Environ.* 238 (2018) 6–18.

[52] C. Lai, M. Wang, G. Zeng, Y. Liu, D. Huang, C. Zhang, R. Wang, P. Xu, M. Cheng, C. Huang, H. Wu, L. Qin, Synthesis of surface molecular imprinted  $\text{TiO}_2$ /graphene photocatalyst and its highly efficient photocatalytic degradation of target pollutant under visible light irradiation, *Appl. Surf. Sci.* 390 (2016) 368–376.

[53] X. Lu, W. Che, X. Hu, Y. Wang, A. Zhang, F. Deng, S. Luo, D.D. Dionysiou, The facile fabrication of novel visible-light-driven Z-scheme  $\text{CuInS}_2/\text{Bi}_2\text{WO}_6$  heterojunction with intimate interface contact by in situ hydrothermal growth strategy for extraordinary photocatalytic performance, *Chem. Eng. J.* 356 (2019) 819–829.

[54] Y. Yuan, P. Wang, Z. Li, Y. Wu, W. Bai, Y. Su, J. Guan, S. Wu, J. Zhong, Z. Yu, Z. Zou, The role of bandgap and interface in enhancing photocatalytic H<sub>2</sub> generation activity of 2D-2D black phosphorus/MoS<sub>2</sub> photocatalyst, *Appl. Catal. B: Environ.* 242 (2019) 1–8.

[55] J. Wang, L. Tang, G. Zeng, Y. Deng, H. Dong, Y. Liu, L. Wang, B. Peng, C. Zhang, F. Chen, 0D/2D interface engineering of carbon quantum dots modified  $\text{Bi}_2\text{WO}_6$  ultrathin nanosheets with enhanced photoactivity for full spectrum light utilization and mechanism insight, *Appl. Catal. B: Environ.* 222 (2018) 115–123.

[56] K. He, G. Chen, G. Zeng, A. Chen, Z. Huang, J. Shi, T. Huang, M. Peng, L. Hu, Three-dimensional graphene supported catalysts for organic dyes degradation, *Appl. Catal. B: Environ.* 228 (2018) 19–28.

[57] R.J. Feng, W.Y. Lei, X.Y. Sui, X.F. Liu, X.Y. Qi, K. Tang, G. Liu, M.H. Liu, Anchoring black phosphorus quantum dots on molybdenum disulfide nanosheets: a 0D/2D nanohybrid with enhanced visible - and NIR - light photoactivity, *Appl. Catal. B: Environ.* 238 (2018) 444–453.

[58] C. Li, H. Liu, Z. Yu, Novel and multifunctional inorganic mixing salt-templated 2D ultrathin Fe/Co-N/S-carbon nanosheets as effectively bifunctional electrocatalysts for Zn-air batteries, *Appl. Catal. B: Environ.* 241 (2019) 95–103.

[59] F. Lei, Y. Sun, K. Liu, S. Gao, L. Liang, B. Pan, Y. Xie, Oxygen vacancies confined in ultrathin indium oxide porous sheets for promoted visible-light water splitting, *J. Am. Chem. Soc.* 136 (2014) 6826–6829.

[60] L. Liang, F. Lei, S. Gao, Y. Sun, X. Jiao, J. Wu, S. Qamar, Y. Xie, Single unit cell bismuth tungstate layers realizing robust solar  $\text{CO}_2$  reduction to methanol, *Angew. Chem. Int. Ed.* 54 (2015) 13971–13974.

[61] P. Xu, G.M. Zeng, D.L. Huang, C.L. Feng, S. Hu, M.H. Zhao, C. Lai, Z. Wei, C. Huang, G.X. Xie, Z.F. Liu, Use of iron oxide nanomaterials in wastewater treatment: a review, *Sci. Total Environ.* 424 (2012) 1–10.

[62] C. Tan, X. Cao, X.-J. Wu, Q. He, J. Yang, X. Zhang, J. Chen, W. Zhao, S. Han, G.-H. Nam, M. Sindoro, H. Zhang, Recent advances in ultrathin two-dimensional nanomaterials, *Chem. Rev.* 117 (2017) 6225–6331.

[63] Y. Yang, C. Zhang, D. Huang, G. Zeng, J. Huang, C. Lai, C. Zhou, W. Wang, H. Guo, W. Xue, R. Deng, M. Cheng, W. Xiong, Boron nitride quantum dots decorated ultrathin porous  $\text{g-C}_3\text{N}_4$ : intensified exciton dissociation and charge transfer for promoting visible-light-driven molecular oxygen activation, *Appl. Catal. B: Environ.* 245 (2019) 87–99.

[64] T. He, S.M. Chen, B. Ni, Y. Gong, Z. Wu, L. Song, L. Gu, W.P. Hu, X. Wang, Zirconium-porphyrin-based metal-organic framework hollow nanotubes for immobilization of noble-metal single atoms, *Angew. Chem. Int. Ed.* 57 (2018) 3493–3498.

[65] S. Kundu, A. Patra, Nanoscale strategies for light harvesting, *Chem. Rev.* 117 (2017) 712–757.

[66] X. Wu, L. Wen, K. Lv, K. Deng, D. Tang, H. Ye, D. Du, S. Liu, M. Li, Fabrication of  $\text{ZnO}/\text{graphene}$  flake-like photocatalyst with enhanced photoreactivity, *Appl. Surf. Sci.* 358 (2015) 130–136.

[67] S. Mandal, S.K. Nayak, S. Mallampalli, A. Patra, Surfactant-assisted porphyrin based hierarchical nano/micro assemblies and their efficient photocatalytic behavior, *ACS Appl. Mater. Interfaces* 6 (2014) 130–136.

[68] R.J. White, N. Yoshizawa, M. Antonietti, M.-M. Titirici, A sustainable synthesis of nitrogen-doped carbon aerogels, *Green Chem.* 13 (2011) 2428–2434.

[69] J. Fu, Q. Xu, J. Low, C. Jiang, J. Yu, Ultrathin 2D/2D  $\text{WO}_3/\text{g-C}_3\text{N}_4$  step-scheme H<sub>2</sub>-production photocatalyst, *Appl. Catal. B: Environ.* 243 (2019) 556–565.

[70] Y. Cao, W. Si, Q. Hao, Z. Li, W. Lei, X. Xia, J. Li, F. Wang, Y. Liu, One-pot fabrication of Hemin-NC composite with enhanced electrocatalysis and application to H<sub>2</sub>O<sub>2</sub> sensing, *Electrochim. Acta* 261 (2018) 206–213.

[71] Y. Deng, L. Tang, G. Zeng, J. Wang, Y. Zhou, J. Tang, L. Wang, C. Feng, Facile fabrication of mediator-free Z-scheme photocatalyst of phosphorous-doped ultrathin graphitic carbon nitride nanosheets and bismuth vanadate composites with enhanced tetracycline degradation under visible light, *J. Colloid Interface Sci.* 509 (2018) 219–234.

[72] Y. Yang, Z. Zeng, C. Zhang, D. Huang, G. Zeng, R. Xiao, C. Lai, C. Zhou, H. Guo, W. Xue, M. Cheng, W. Wang, J. Wang, Construction of iodine vacancy-rich  $\text{BiOI}/\text{Ag@AgI}$  Z-scheme heterojunction photocatalysts for visible-light-driven tetracycline degradation: transformation pathways and mechanism insight, *Chem. Eng. J.* 349 (2018) 808–821.

[73] L. Tang, J. Wang, G. Zeng, Y. Liu, Y. Deng, Y. Zhou, J. Tang, J. Wang, Z. Guo, Enhanced photocatalytic degradation of norfloxacin in aqueous  $\text{Bi}_2\text{WO}_6$  dispersions containing nonionic surfactant under visible light irradiation, *J. Hazard. Mater.* 306 (2016) 295–304.

[74] J. Wang, L. Tang, G. Zeng, Y. Deng, Y. Liu, L. Wang, Y. Zhou, Z. Guo, J. Wang, C. Zhang, Atomic scale  $\text{g-C}_3\text{N}_4/\text{Bi}_2\text{WO}_6$  2D/2D heterojunction with enhanced photocatalytic degradation of ibuprofen under visible light irradiation, *Appl. Catal. B: Environ.* 209 (2017) 285–294.

[75] L. Ge, J. Chen, S. Zhang, X. Cai, Z. Wang, C. Wang, Photodegradation of fluorquinolone antibiotic gatifloxacin in aqueous solutions, *Chin. Sci. Bull.* 55 (2010) 1495–1500.

[76] W. Zhang, G. Li, H. Liu, J. Chen, S. Ma, T. An, Micro/nano-bubble assisted synthesis of  $\text{Au}/\text{TiO}_2@\text{CNTs}$  composite photocatalyst for photocatalytic degradation of gaseous styrene and its enhanced catalytic mechanism, *Environ. Sci. Nano* (2019), <https://doi.org/10.1039/C8EN01375F>.

[77] P. Wang, Z. Shen, Y. Xia, H. Wang, L. Zheng, W. Xi, S. Zhan, Atomic insights for optimum and excess doping in photocatalysis: a case study of few-layer Cu-ZnIn<sub>2</sub>S<sub>4</sub>, *Adv. Funct. Mater.* 29 (2019) 1807013.

[78] S. Luo, J. Ke, M. Yuan, Q. Zhang, P. Xie, L. Deng, S. Wang, CuInS<sub>2</sub> quantum dots embedded in  $\text{Bi}_2\text{WO}_6$  nanoflowers for enhanced visible light photocatalytic removal of contaminants, *Appl. Catal. B: Environ.* 221 (2018) 215–222.

[79] R.F.P. Nogueira, M.C. Oliveira, W.C. Paterlini, Simple and fast spectrophotometric determination of H<sub>2</sub>O<sub>2</sub> in photo-Fenton reactions using metavanadate, *Talanta* 66 (2005) 86–91.

[80] L.G. Devi, M.L. ArunaKumari, Enhanced photocatalytic performance of hemin (chloro(proto porphyrinato)iron(III)) anchored  $\text{TiO}_2$  photocatalyst for methyl orange degradation: a surface modification method, *Appl. Surf. Sci.* 276 (2013) 521–528.